Control of Turbulent Transport in Supercritical Currents by Three Families of Hairpin Vortices

Jorge S. Salinas* and S. Balachandar†
Department of Mechanical and Aerospace Engineering, University of Florida, Gainesville, FL. USA

M. I. Cantero
Instituto Balseiro. Consejo Nacional de Investigaciones Científicas y Técnicas. and Centro Atómico Bariloche, Comisión Nacional de Energía Atómica, San Carlos de Bariloche, Argentina.

We elucidate the turbulent structure of supercritical gravity currents by means of highly-resolved simulations that employ up to a billion grid points. Three families of hairpin vortices dominate the near-bed and interface layers of the current, with their generation mechanisms dictating their shape, orientation, and number density. The interaction of near-bed and lower-interface hairpins explains the weak inviscid lid-like behavior of the streamwise velocity maximum, while the upper-interface vortices are responsible for the substantially lower entrainment compared to turbulent wall-jets.

Gravity currents are buoyancy driven flows that flow over a surface, where the density difference between the current and the ambient can be due to differences in temperature, salinity or suspended sediments (i.e. turbidity currents). Here we explore the particular case of a conservative gravity current or equivalently a turbidity current carrying very fine sediment. Specifically, we focus on supercritical currents whose densimetric Froude number is larger than unity [1]. Supercritical currents are similar to turbulent wall-jets (TWJs) in that they are comprised of a near-bed layer and an interface layer separated at the maximum of streamwise velocity. However, the downstream development of supercritical gravity currents is substantially different due to the presence of stable stratification - the growth of supercritical currents in the bed-normal direction is observed to be five times lower than that of TWJs [2–4]. An important consequence of this much lower rate of entrainment of ambient fluid is that supercritical currents can extend over long streamwise distances without being diluted by strong mixing with the ambient.

We address the following fundamental question in this letter: how does stratification alter the structure of turbulence within the near-bed and interface layers to achieve the substantially lower entrainment rate. Furthermore, it has been observed that the near-bed layer of a gravity current behaves as a turbulent channel capped by an upper lid, in contrast to the near-bed layer of a TWJ whose behavior is akin to that of a freely growing turbulent boundary layer (TBL) [5]. Explaining this observation in terms of the subtle interaction between the near-bed and the shear-layer turbulent structures at the overlap region is an important focus of the present work. We seek to present a composite picture with detailed structural and statistical analysis of a highly-resolved simulation that employs up to a billion grid points [6, 7].

Simulation Details – Results from a highly-resolved direct simulation of a supercritical current of Froude number $Fr = 2.65$ flowing down a bed of slope $\theta = 2.86°$ is analyzed. Thus, the simulation models a streamwise segment of the long body of a current, away from the energetic front and the weak tail. The concentration of sediment is taken to be dilute, which allows Boussinesq approximation. Suspended sediment is assumed to be sufficiently small in size that its settling effect is ignored

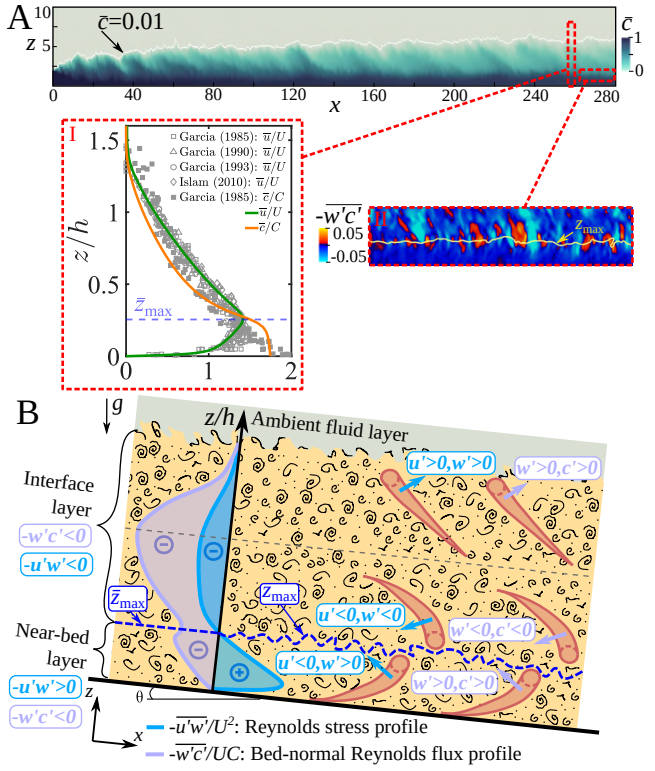

FIG. 1. (A) Spanwise averaged concentration field at one instant in time. Inset I: $\overline{u}/U$ and $\overline{c}/C$ as a function of z/h along with experimental data [8–11]. (B) Schematic representation of a supercritical current. The location of the velocity maximum is depicted (dashed blue line) together with Reynolds stress and flux profiles.

and treated as washload. The conservation equations of fluid mass, momentum and sediment concentration are as given in [2, 3]. The results to be discussed are non-dimensionalized with the half-height H of the current at the inlet as the length scale, average concentration c_v at the inlet as the concentration scale, and $u_* = \sqrt{g' \sin\theta H}$ as the scale of the velocity field $\mathbf{u} = \{u, v, w\}$ [2]. Here $g' = Rc_v g$ is the reduced gravity with g being the acceleration due to gravity, and $R = \rho_s/\rho_f - 1$, where the density of sediment and clear fluid are ρ_s and ρ_f, respectively. The dimensionless parameters are the shear Reynolds number $Re_\tau = u_* H/\nu = 180$ and the Schmidt number $Sc = \nu/\kappa = 1$. Here ν is the kinematic viscosity and κ is the sediment diffusivity.

Structure of Supercritical Current – Fig. 1A shows the spanwise averaged concentration field $\overline{c}$ at one instant in time. The thickness of the current, identified as the white contour of $\overline{c} = 0.01$, increases downstream as the current entrains ambient fluid at the top. Inset I in Fig. 1A presents the scaled streamwise velocity $\overline{u}/U$ and concentration $\overline{c}/C$ as a function of scaled bed-normal location z/h. Here we use the integral scales U, C and h as defined in [12, 13]. We see good agreement between the experimental [8–11] (symbols) and simulation results for both mean velocity and concentration (lines). Fig. 1B shows a schematic of a supercritical current to be comprised of an interface layer and a near-bed layer that merge in an overlap region at the maximum of streamwise velocity (dashed blue line).

Three Families of Hairpin Vortices – Fig. 2 shows a composite plot of the vortical structure of the current dominated by three families of hairpin-like vortices captured by isosurfaces of swirling strength ($\lambda_{ci} = 5$, [14]) and colored by bed normal location z, together with an isosurface of $c = 0.01$ (light brown) for half of the domain. Three distinct regions can be found: (i) the near-bed layer, below the maximum of streamwise velocity, populated by hairpin vortices with their heads pointing up and forward (see top view in Fig. 2A); (ii) lower-interface region, above the maximum of streamwise velocity, populated by upside-down hairpin vortices with their heads pointing down and forward (see bottom view in Fig. 2B); (iii) upper-interface region, near the current-ambient interface, populated by hairpin vortices with their heads pointing up and backwards (see top view in Fig. 2C). These structures are coherent in time, until they stretch and break up into smaller-scale turbulence.

Figs. 2A-C show three/four close-up views of one hairpin vortex from each family (panels numbered by roman numerals), with isosurfaces of Reynolds stress $-u'w'$ (light blue in panels II) and bed-normal Reynolds flux $-w'c'$ (light violet and brown in panels III and IV). Note that in each figure the axes are oriented differently to see the vortices in the same perspective. Also, we show contours of perturbations from the mean (u', w', c') and cross-correlations ($-u'w'$, $-u'c'$, $-w'c'$) at a $y-z$ plane going through the middle of the corresponding turbulent structure (dashed red planes), together with contours of $\lambda_{ci} = 5$ (green), the location of the streamwise velocity maximum (white contours in Fig. 2A-B) and the interface location (white contours of $c = 0.01$ in Fig. 2C). Both legs of each vortex are marked by green crosses. Focusing on the ejection zone of the near-bed hairpin vortex between the legs (Fig. 2A) we see that $u' < 0$, while $w' > 0$ and $c' > 0$. This results in positive Reynolds stress ($-u'w' > 0$ – panel II) and negative Reynolds flux ($-u'c' < 0$,$-w'c' < 0$ – panel III). In the ejection region of the lower-interface hairpin (Fig. 2B), u', w' and c' are all negative, which results in $-u'w' < 0$ (panel II), $-w'c' < 0$ (panel III) and $-u'c' > 0$. The same can be found in the ejection zone of the upper-interface hairpin vortex (Fig. 2C), although produced by all positive values of u', w' and c'. A schematic summary of the three families is presented in Fig. 1B along with Reynolds stress and flux profiles. All three families contribute to momentum and concentration transport down the velocity and concentration gradient, respectively.

We present isosurfaces of constant streamwise vorticity Ω_x (light yellow and pink – panels II) and bed-normal vorticity Ω_z (light green and cyan – panels III; see color scale at bottom left of Figs. 2A-C). Apart from orientation, there are differences in the shape of the three hairpin structures due to differences in the instability mechanism that generated them. The auto-generation mechanism of near-bed hairpin vortices has been elaborated in [15, 16] and shear layer instability is responsible for the generation of upper-interface hairpins. In comparison, the production mechanism of the lower-interface vortices is less well studied. Differences in the mean velocity curvature plays an important role in the respective instabilities and determine the shape and orientation of the hairpins. The induced velocity of the near-bed hairpin head and legs is to lift it up and backward with respect to the mean flow (see Fig. 2D). The induced velocity of the lower-interface hairpin is to push it down towards the velocity maximum and backward. The interaction between these two families of vortices defines the structure of the current near the streamwise velocity maximum. The induced velocity of the upper-interface hairpin is to lift it up and forward and plays a central role in entrainment.

Control of Turbulent Transport – Fig. 3A shows the spanwise-time averaged mean streamwise velocity profile scaled by $\overline{u}_\tau$ as a function of bed-normal location $z^+ = Re_\tau \overline{u}_\tau z$, where $\overline{u}_\tau$ is the local shear velocity computed from the bed-normal gradient of streamwise velocity at the bed. The vertical dashed gray line indicates the location of velocity maximum. Fig. 3B shows $\overline{u}^+_{\rm rms} = \sqrt{\overline{u'u'}}/\overline{u}_\tau$, $\overline{v}^+_{\rm rms} = \sqrt{\overline{v'v'}}/\overline{u}_\tau$, $\overline{w}^+_{\rm rms} = \sqrt{\overline{w'w'}}/\overline{u}_\tau$, $\overline{c}_{\rm rms}/\overline{c}_b = \sqrt{\overline{c'c'}}/\overline{c}_b$, $\overline{u'w'}^+ = \overline{u'w'}/\overline{u}^2_\tau$ and $-Ri_\tau \overline{w'c'}/(\overline{u}_\tau \overline{c}_b)$ as a function of bed-normal location z^+, where $\overline{c}_b$ is the concentration at the bottom bed. Two

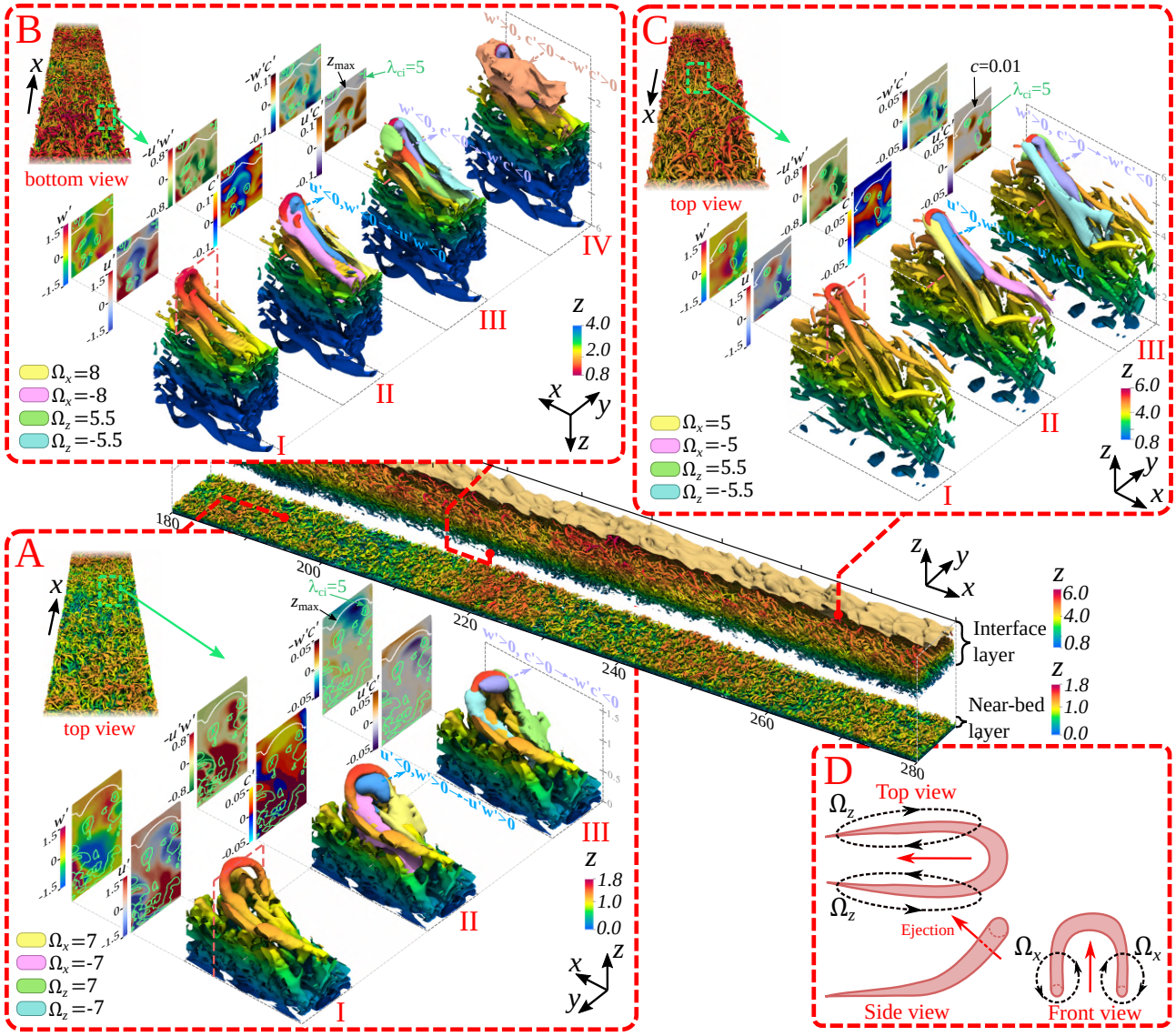

FIG. 2. Isosurface of swirling strength ($\lambda_{ci} = 5$) and colored by bed normal location z (see different scales), together with an isosurface of $c = 0.01$ (light brown) for half of the domain. Three/four close-up views of an example hairpin structure within the (A) near-bed, (B) lower-interface, and (C) upper-interface regions are shown. In A-C we also show contours of velocity and concentration perturbations and cross-correlations on a $y - z$ plane going through the middle of the hairpin (dashed red planes), together with contours of $\lambda_{ci} = 5$ (green). Also, we show isosurfaces of $-u'w'$ (light blue), $-w'c'$ (light violet and brown), bed-normal vorticity Ω_z (light green and cyan) and streamwise vorticity Ω_x (light yellow and pink). (D) Schematic of a hairpin vortex.

local maxima of $\overline{u}^+_{\rm rms}$, $\overline{v}^+_{\rm rms}$ and $\overline{w}^+_{\rm rms}$ can be seen, one in the near-bed and another in the interface layers. The minima of $\overline{u}^+_{\rm rms}$ is located at the maximum of streamwise velocity $\overline{z}^+_{\rm max} = 210$, while the minima of $\overline{v}^+_{\rm rms}$ and $\overline{w}^+_{\rm rms}$ and the maxima of $\overline{c}_{\rm rms}$ are slightly above at $z^+ \approx 236$, 271 and 235. The zero-crossing of Reynolds stress is at $z^+ \approx 212$, which means that shear production of turbulent kinetic energy (TKE) is negative in a small region ($210 < z^+ \lessapprox 212$). However, as noted in [5], total TKE production remains positive almost everywhere. The bed-normal Reynolds flux (light green profile) remains negative across the entire current.

In Figs. 3A,B we compare the mean and rms velocity profiles with those from TWJs [4, 17], TBL [18] and turbulent channel flow (TCF) [19]. It is quite striking that in the near-bed region the closest comparison of the supercritical flow is with TCF. Some deviations in terms of higher velocity fluctuations near the velocity maximum can be observed for the supercritical current, due to the asymmetric nature of the mean velocity profile as compared to TCF. The rms velocity fluctuations are generally much higher in the case of TBL and TWJ. The most

important inference to be drawn is that the surface of velocity maximum acts like a weak inviscid lid, somewhat similar to the mid-plane of a TCF, and as a result, the streamwise growth of the near-bed layer of a supercritical current is much slower than in TBL or TWJ. The difference from TWJ is clearly due to stable stratification.

An important feature of the velocity maximum is the existence of a local lutocline-like large concentration gradient, whose origin will be explored below. As the hairpin vortices encroach upward and downward, they give the surface of streamwise velocity maximum an undulating character (see yellow contour of $z_{\max}$ in inset II of Fig. 1A). The near-bed (lower-interface) hairpins pump high (low) concentration fluid up (down) between their legs contributing to negative Reynolds flux. However, an important characteristic of these hairpins is the existence of a stagnation point [16], where the backward ejected fluid (with respect to the moving hairpin) meets the forward moving fluid. Across the stagnation point, while the bed-normal velocity perturbations change sign, the concentration fluctuations continue to be positive (negative) for the near-bed (lower-interface) hairpins. As regions of high (low) concentration are pushed beyond the stagnation points, counter-gradient fluxes form slightly upstream of the hairpin heads (see light brown isosurface in panel IV of Fig. 2B) contributing to sharpening of the concentration gradient.

The lower-interface hairpins are somewhat fewer and of lower intensity than the near-bed hairpins. Furthermore, though the spatio-temporal correlation between the two is weak, we observe the head of the lower-interface hairpins to be located slightly downstream of the near-bed hairpin heads (see the schematic in Figure 1B). Partly due to this arrangement, and partly due to the stronger concentration gradient above the velocity maximum, the regions of strong counter-gradient concentration flux are observed to be associated with the lower-interface hairpins. The span-time average performed for Fig. 3 are at constant (x, z) locations and therefore the r.m.s values evaluated at $\overline{z}^+_{\max}$ do not truly reflect the behavior at the local velocity maximum, due to the undulating nature of z_{max} (see inset II in Fig. 1A). Nevertheless, the combined effect of the near-bed and lower-interface hairpin vortices creates alternate patches of high and low concentration, which are responsible for the peak in $\overline{c}_{rms}$ and the near constant negative Reynolds flux.

The mean streamwise momentum simplifies to [4, 13, 20]

$$-\frac{\partial \overline{p}}{\partial x} + \frac{1}{Re_\tau}\frac{\partial^2 \overline{u}}{\partial z^2} - \frac{\partial}{\partial z}\overline{u'w'} + \overline{c} - \frac{\partial \overline{u^2}}{\partial x} - \frac{\partial \overline{u}\,\overline{w}}{\partial z} = 0, \quad (1)$$

whose terms scaled by $1/(Re_\tau \overline{u}^3_\tau)$ are shown in Fig. 3C. The concentration $\overline{c}$ (solid black profile) is the primary source of momentum, which in the region $z^+ \lessapprox 150$, is balanced by both the gradient of Reynolds stress (solid red) and viscous diffusion (dashed red), following the classical behavior of a TCF. The most interesting balance is in the interface layer, where $\overline{c}$ is not entirely balanced by Reynolds and viscous stresses. For ($z^+ \gtrapprox 80$) part of the driving force goes to increasing the kinetic energy of the mean streamwise flow (blue profile). This slow streamwise acceleration of the fluid only in the region close to and above the velocity maximum is consistent with the TCF-like evolution of the near-bed layer. Thus, the streamwise growth of a supercritical current is mostly due to the thickening of the interface layer, with only a weak growth of the near-bed layer. Close to the interface ($600 \lessapprox z^+ \lessapprox 1200$, inset I) we see a balance between vertical transport of mean streamwise momentum ($-\overline{u}\,\overline{w}$) and Reynolds stress ($-\overline{u'w'}$), indicating that the transport of turbulent eddies upward near the interface enables incorporation of ambient fluid into the mean motion of the current, which is the hallmark of the entrainment process.

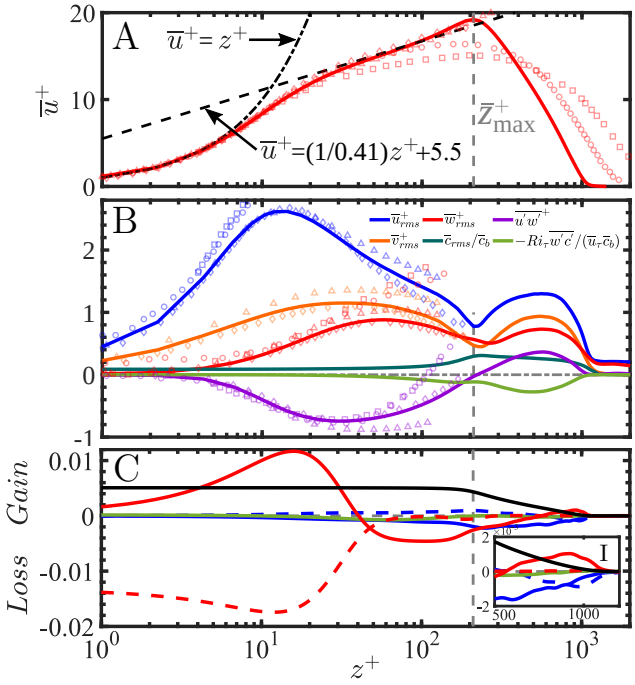

FIG. 3. (A) $\overline{u}^+$ as a function of z^+. (B) Scaled r.m.s and cross-correlations as a function of z^+. (C) Scaled mean streamwise momentum balance as a function of z^+. (▬), $-\frac{\partial \overline{u}^2}{\partial x}$; (▬ ▬), $-\frac{\partial \overline{u}\,\overline{w}}{\partial z}$; (▬), $-\frac{\partial \overline{p}}{\partial x}$; (▬ ▬), $\frac{1}{Re_\tau}\frac{\partial^2 \overline{u}}{\partial z^2}$; (▬), $-\frac{\partial}{\partial z}\overline{u'w'}$; (▬), $\overline{c}$. Also plotted are results from DNS of TWJ [4] (○), Experiments of TWJ [17] (□), DNS of TBL [18] (△), and DNS of TCF [19] (◇). Colors of each term in the data are the same as described above.

Discussion – When comparing the supercritical current with the TWJ, the most striking difference is at the velocity maximum, where the interplay between the local turbulent vortical structures and the sediment concentration drastically alters the overall turbulent transport. In a supercritical current, we observe a "feedback loop" with

the persistent counter-gradient transport induced by the interacting hairpin vortices increasing the local concentration gradient and the local high concentration gradient then, in turn, modulating turbulent structures in the lower-interface region. We conjecture that this modified behavior at the velocity maximum also plays an important role in the less intense nature of the upper-interface hairpins in a supercritical current compared to TWJ. As a result of these interactions, the entrainment rate (or the growth rate) of a supercritical current is about five times lower than that of a TWJ [2].

The supercritical gravity current can also be compared with the subcritical counterpart [5], with the latter now seen as an extreme case. In the subcritical case, the lower-interface vortices consist only of a weak head with no quasi-streamwise vortex legs. This results in a substantial region of both counter-gradient concentration flux and counter-gradient Reynolds stress. As a result, the near-bed layer of a subcritical current is fully capped by a strong lutocline and the interface layer becomes turbulence-free. Since there are no upper-interface hairpin vortices, a subcritical current grows very slowly only by viscous diffusion. In this sense, the structure of a supercritical current is between those of a TWJ and a subcritical current.

* josalinas@ufl.edu
† bala1s@ufl.edu

[1] J. Salinas, S. Balachandar, M. Shringarpure, J. Fedele, D. Hoyal, and M. Cantero, Proceedings of the National Academy of Sciences **117**, 18278 (2020).
[2] J. S. Salinas, M. Cantero, M. Shringarpure, and S. Balachandar, Journal of Geophysical Research: Oceans **124**, 7989 (2019).
[3] J. S. Salinas, M. Cantero, M. Shringarpure, and S. Balachandar, Journal of Geophysical Research: Oceans **124**, 8017 (2019).
[4] I. Z. Naqavi, J. C. Tyacke, and P. G. Tucker, Journal of Fluid Mechanics **852**, 507 (2018).
[5] J. Salinas, S. Balachandar, M. Shringarpure, J. Fedele, D. Hoyal, S. Zuniga, and M. Cantero, Nature Communications (In Print).
[6] A. T. Patera, Journal of Computational Physics **54**, 468 (1984).
[7] P. Fischer, J. Lottes, and S. Kerkemeier, Available at: http://nek5000.mcs.anl.gov.
[8] M. García, *Experimental study of turbidity currents*, M. S. thesis, University of Minnesota, Minneapolis, Minnesota, USA (1985).
[9] M. García, *Depositing and eroding sediment-driven flows: turbidity currents*, Ph.D. thesis, University of Minnesota, St. Anthony Falls Hydraulic Laboratory (1990).
[10] M. García and G. Parker, Journal of Geophysical Research **98**, 4793 (1993).
[11] M. A. Islam and J. Imran, Journal of Geophysical Research: Oceans **115** (2010).
[12] T. Ellison and J. Turner, Journal of Fluid Mechanics **6**, 423 (1959).
[13] G. Parker, Y. Fukushima, and H. Pantin, Journal of Fluid Mechanics **171**, 145 (1986).
[14] P. Chakraborty, S. Balachandar, and R. Adrian, Journal of Fluid Mechanics **535**, 189 (2005).
[15] J. Zhou, R. J. Adrian, and S. Balachandar, Physics of Fluids **8**, 288 (1996).
[16] J. Zhou, R. Adrian, S. Balachandar, and T. Kendall, Journal of Fluid Mechanics **387**, 353 (1999).
[17] E. P. Gnanamanickam, S. Bhatt, S. Artham, and Z. Zhang, Journal of Fluid Mechanics **877**, 239 (2019).
[18] P. R. Spalart, Journal of Fluid Mechanics **187**, 61 (1988).
[19] M. Lee and R. D. Moser, Journal of Fluid Mechanics **774**, 395–415 (2015).
[20] M. Shringarpure, M. I. Cantero, and S. Balachandar, Journal of Fluid Mechanics **712**, 384 (2012).